

Biophysical principles of choanoflagellate self-organization

Ben T. Larson^{a,b,c}, Teresa Ruiz-Herrero^d, Stacey Lee^e, Sanjay Kumar^{e,f} , L. Mahadevan^{d,g,h,i,1} , and Nicole King^{a,b,1} 

^aHoward Hughes Medical Institute, University of California, Berkeley, CA 94720; ^bDepartment of Molecular and Cell Biology, University of California, Berkeley, CA 94720; ^cBiophysics Graduate Group, University of California, Berkeley, CA 94720; ^dPaulson School of Engineering and Applied Sciences, Harvard University, Cambridge, MA 02138; ^eUniversity of California, Berkeley–University of California, San Francisco Graduate Program in Bioengineering, Department of Bioengineering, University of California, Berkeley, CA 94720; ^fDepartment of Chemical and Biomolecular Engineering, University of California, Berkeley, CA 94720; ^gDepartment of Physics, Harvard University, Cambridge, MA 02138; ^hDepartment of Organismic and Evolutionary Biology, Harvard University, Cambridge, MA 02138; and ⁱKavli Institute for NanoBio Science and Technology, Harvard University, Cambridge, MA 02138

Edited by Thomas D. Pollard, Yale University, New Haven, CT, and approved December 4, 2019 (received for review June 4, 2019)

Inspired by the patterns of multicellularity in choanoflagellates, the closest living relatives of animals, we quantify the biophysical processes underlying the morphogenesis of rosette colonies in the choanoflagellate *Salpingoeca rosetta*. We find that rosettes reproducibly transition from an early stage of 2-dimensional (2D) growth to a later stage of 3D growth, despite the underlying variability of the cell lineages. Our perturbative experiments demonstrate the fundamental importance of a basally secreted extracellular matrix (ECM) for rosette morphogenesis and show that the interaction of the ECM with cells in the colony physically constrains the packing of proliferating cells and, thus, controls colony shape. Simulations of a biophysically inspired model that accounts for the size and shape of the individual cells, the fraction of ECM, and its stiffness relative to that of the cells suffices to explain our observations and yields a morphospace consistent with observations across a range of multicellular choanoflagellate colonies. Overall, our biophysical perspective on rosette development complements previous genetic perspectives and, thus, helps illuminate the interplay between cell biology and physics in regulating morphogenesis.

morphogenesis | multicellularity | morphospace | quantitative cell biology | extracellular matrix

Nearly all animals start life as a single cell (the zygote) that, through cell division, cell differentiation, and morphogenesis, gives rise to a complex multicellular adult form (1, 2). These processes in animals require regulated interplay between active cellular processes and physical constraints (3–9). A particularly interesting system in which to study this interplay is the choanoflagellates, the closest relatives of animals (10–12). Choanoflagellates are aquatic microbial eukaryotes whose cells bear a diagnostic “collar complex” composed of an apical flagellum surrounded by an actin-filled collar of microvilli (13, 14) (Fig. 1). The life histories of many choanoflagellates involve transient differentiation into diverse cell types and morphologies (15, 16). For example, in the model choanoflagellate *Salpingoeca rosetta*, solitary cells develop into multicellular colonies through serial rounds of cell division (17), akin to the process by which animal embryos develop from a zygote (Fig. 14). Therefore, choanoflagellate colony morphogenesis presents a simple, phylogenetically relevant system for investigating multicellular morphogenesis from both a biological and a physical perspective (14). *S. rosetta* forms planktonic, rosette-shaped colonies (“rosettes”), in which the cells are tightly packed into a rough sphere that resembles a morula-stage animal embryo (17). Because the cell-division furrow forms along the apical–basal axis, thereby dissecting the collar, all of the cells in rosettes are oriented with their flagella and collars facing out into the environment and their basal poles facing into the rosette interior (Fig. 1 *B* and *C*). Interestingly, all 3 genes known to be required for rosette development are regulators of the extracellular matrix (ECM): a C-type lectin called *rosetteless* (18) and 2 predicted glycosyltransferases called *jumble*

and *couscous* (19). Nonetheless, little is known about either the mechanistic role of the ECM or the extent to which rosette morphogenesis is shaped by physical constraints.

A critical barrier to understanding the biological and physical mechanisms underlying rosette morphogenesis has been the absence of a detailed characterization of the morphogenetic process. For example, it is not known whether rosettes form through the development of invariant cell lineages akin to those seen in *Caenorhabditis elegans* (20) or through variable cell divisions, as occurs, for example, in sponges and mice (21, 22). Moreover, it is not known whether there are identifiable developmental stages in rosette development. To quantify the principles of rosette morphogenesis, we used a combination of quantitative descriptions of rosette development, experimental perturbations, and biophysical simulations that together reveal the importance of the regulated secretion of basal ECM in physically constraining proliferating cells and thereby sculpting choanoflagellate multicellularity.

Results

Rosette Morphogenesis Displays a Stereotyped Transition from 2-Dimensional to 3-Dimensional Growth. To constrain our search for mechanistic principles, we first quantified the range of sizes and spectrum of morphologies of *S. rosetta* rosettes by measuring

Significance

Comparisons among animals and their closest living relatives, the choanoflagellates, have begun to shed light on the origin of animal multicellularity and development. Here, we complement previous genetic perspectives on this process by focusing on the biophysical principles underlying choanoflagellate colony morphology and morphogenesis. Our study reveals the crucial role of the extracellular matrix in shaping the colonies and leads to a phase diagram that delineates the range of morphologies as a function of the biophysical mechanisms at play.

Author contributions: B.T.L., T.R.-H., S.L., S.K., L.M., and N.K. designed research; B.T.L., T.R.-H., and S.L. performed research; B.T.L. and T.R.-H. contributed new reagents/analytic tools; B.T.L., T.R.-H., and S.L. analyzed data; and B.T.L., T.R.-H., S.L., S.K., L.M., and N.K. wrote the paper.

The authors declare no competing interest.

This article is a PNAS Direct Submission.

This open access article is distributed under Creative Commons Attribution-NonCommercial-NoDerivatives License 4.0 (CC BY-NC-ND).

Data deposition: Code for simulations is available at https://github.com/truizherrero/choanoflagellate_colonies.

¹To whom correspondence may be addressed. Email: lmahadev@g.harvard.edu or nking@berkeley.edu.

This article contains supporting information online at <https://www.pnas.org/lookup/suppl/doi:10.1073/pnas.1909447117/-DCSupplemental>.

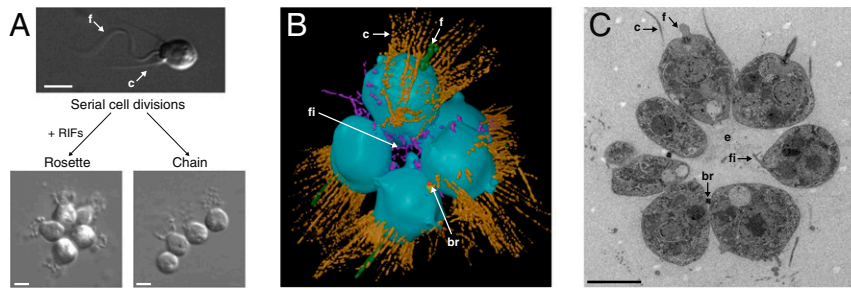


Fig. 1. *S. rosetta* develops from a single cell into multicellular colonies through serial rounds of cell division. (A) All choanoflagellate cells bear a diagnostic “collar complex” composed of an apical flagellum (f) surrounded by an actin-filled collar of microvilli (c) (13, 14). *S. rosetta* produces 2 different colonial forms: compact, mechanically robust, roughly spherical rosette colonies (Rosette) that form in the presence of bacterial Rosette Inducing Factors (RIFs; refs. 17, 23, and 24); and fragile, linear chain colonies (Chain) that form during rapid cell growth in the absence of RIFs (16). Both types of colonies form by serial cell divisions. Reprinted from ref. 16. Copyright (2011) with permission from Elsevier. Reprinted from ref. 19, which is licensed under CC BY 4.0. (B) A 3D reconstruction of a rosette (from ref. 37). Cells (blue) in rosettes are packed around a central focus with apical collars (c; orange) and flagella (f; green) facing into the environment. Some cells are connected by cytoplasmic bridges (br; red) (37), which are also observed in chains (16). Filopodia (fi; purple) extend into the center of rosettes, which is devoid of cells (18). Reprinted from ref. 37, which is licensed under CC BY 4.0. (C) Thin section through the equator of a rosette, imaged by transmission electron microscopy, illustrates the subcellular architecture of a rosette (37). Labeled as in B. (Scale bars, 3 μ m.)

the population-wide distribution of rosette size in terms of cell number. Following previous work, we defined rosettes starting at the 4-cell stage, although cells can be found as singlets, doublets, and triplets as well. *S. rosetta* cultured solely in the presence of the rosette-inducing bacterium *Algoriphagus machipongonensis* (23) led to a population in which the distribution of cells per individual was stationary (i.e., unchanging over time), where an “individual” refers to any unicell or group of cells including rosettes. While some rosettes contained as many as 25 cells, the most common rosette size was 8 cells per rosette, with 51% of rosettes containing between 6 and 8 cells (Fig. 2A). While rosettes grow through cell division, their ultimate size is determined by either colony fission (as reported; ref. 16) or cell extrusion (SI Appendix, Fig. S1). In each case, the rosettes contained 8 or more cells, suggesting that these rosette size-decreasing phenomena are more common in larger rosettes.

We next quantified defining features of the 3-dimensional (3D) morphology of rosettes containing between 4 (the smallest cell number clearly identifiable as a rosette; ref. 24) and 12 cells (representing 90% of rosettes at steady state; SI Appendix, Materials and Methods and Fig. 2B and C). This analysis revealed that rosettes increased in volume and diameter as cell number increased (Fig. 2D). Although the average cell volume reduced between the 4- and 5-cell stages of rosette development, average cell volume did not change substantially with increasing cell number after the 5-cell stage (SI Appendix, Fig. S2), suggesting that cells in rosettes grow between cell divisions. This contrasts with cleavage in the earliest stages of animal embryogenesis, in which cell volume steadily decreases as cell divisions proceed with no cell or overall tissue growth (2).

Our analyses revealed that rosette morphogenesis displays 2 distinct, but previously undescribed, phases: 1) a 2D phase of growth from 4 to 7 cells, during which the overall shape of rosettes changed substantially with increasing cell number; and 2) a 3D phase from 8 to 12 cells, during which rosettes expanded nearly isotropically (Fig. 2C–E). Interestingly, the most common rosette size (8 cells) corresponded to the transition between the 2 phases of growth.

Transitions from 2D to 3D growth can be driven by the constrained growth of cell layers leading to increasing mechanical stresses (25–29). We hypothesized that the physical packing of cells in rosettes might constrain cell growth and proliferation and help explain the growth transition during rosette morphogenesis. Indeed, cell packing initially increased, as indicated by an increase in the number of nearest neighbor cells (Fig. 2F), and suggested by the reduced average sphericity of cells (SI Appendix,

Fig. S2). Following the growth transition at the 8-cell stage, cell packing continued to increase with increasing cells per rosette, although the rate of increase slowed as a function of the number of cells per rosette (Fig. 2F). Therefore, the transition to isotropic 3D growth in 8-cell rosettes may occur in response to the accumulation of stress caused by the increase in cell packing in growing rosettes.

Rosette Developmental Dynamics Are Variable. The influence of cell packing on rosette morphogenesis did not preclude the possibility that the rosette-developmental program might also involve specific patterns of cell division that result in well-defined cell lineages. We therefore documented cell lineages in live, developing rosettes (Fig. 3). Consistent with the single published observation of live rosette development (17), the cells maintained polarity throughout development, with their division planes oriented along the apical–basal axis. Relative to the cell-division times in linear chains (Fig. 1A), which form when rosette-inducing bacteria are absent, we observed a slight, but statistically significant, increase in division rate in rosettes ($P = 0.03$ by Wilcoxon rank sum test; SI Appendix, Fig. S3A). In addition, we found that both the order and timing of cell divisions differed among different rosettes (Fig. 3B and C), ruling out the possibility that cell lineages are invariant. This process of apparently unpatterned cell divisions resembles the dynamics of early embryogenesis in diverse animals, including sponges and mice (21, 22).

Although division patterns were variable between rosettes, ruling out the possibility of invariant cell lineages, in no rosette did cells from the 1st, 2nd, or 3rd cell division give rise to more than 60% of cells (Fig. 3D). Moreover, cell division remained balanced throughout rosette morphogenesis, with no cell lineage coming to dominate. Importantly, the cell lineages of chains showed the same kind of variability as rosettes (Fig. 3D). These observations suggest that rosette morphogenesis does not require the strongest forms of cell-cycle control or coordination [i.e., the synchronous divisions or deterministic division timing or order observed in the development of some animals such as *C. elegans*, *Xenopus*, *Drosophila*, and zebrafish (30–33) and in the green alga *Volvox* (34–36)].

ECM Constrains Proliferating Cells in Rosettes. To reconcile the stereotyped 3D growth transition (Fig. 2) with the variable developmental dynamics of rosette formation (Fig. 3), we set out to test the “ECM constraint hypothesis” (Fig. 4A and B). This hypothesis was motivated by the idea that physical constraints imposed by the geometry and mechanics of cell packing play a

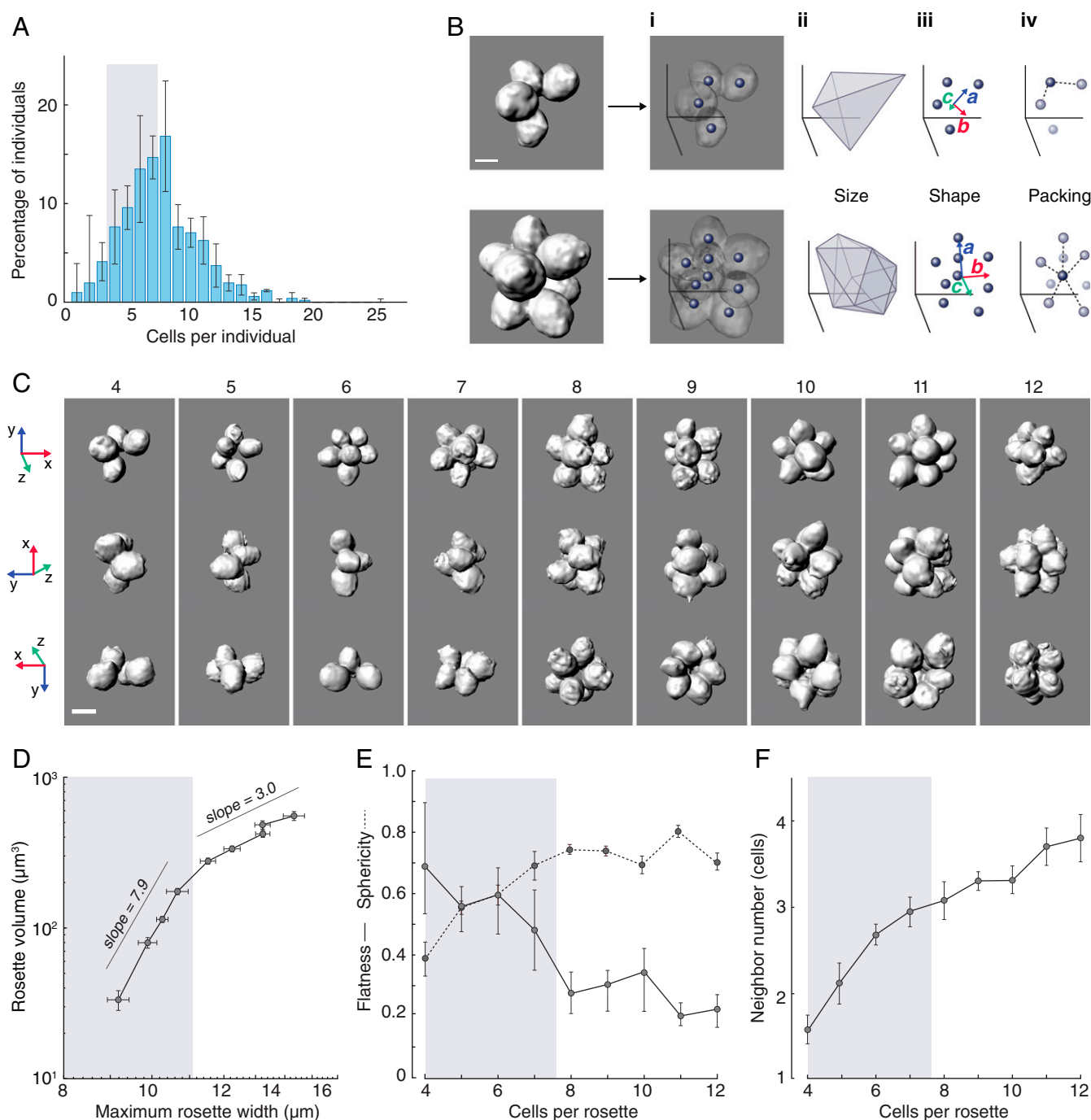


Fig. 2. Quantitative analysis of rosette morphology reveals that rosettes undergo a reproducible 2D to 3D growth transition. (A) Under conditions of constant rosette induction, *S. rosetta* existed as unicells, doublets, triplets, and rosettes containing between 4 and 25 cells, with the most common rosette size being 8 cells per individual. Following previous work (24), we defined 4 cells as the smallest number clearly identifiable as a rosette. Each unicell or group of cells was considered an “individual.” The mean percentage of individuals in a population (y axis) was plotted by number of cells per individual (x axis). Error bars indicate SDs of measurements from 3 different days. $n = 511$ individuals. Gray background indicates rosettes of 4 to 7 cells (D and E). (B) Image-analysis pipeline for quantitatively comparing rosette morphologies is illustrated here for 2 representative rosettes. For each rosette, cell positions (dots) were extracted (B, i) and used to determine rosette size, including volume (measured by convex hull) (B, ii), shape, including flatness and sphericity (the former quantified by $1 - c/b$ and the latter by $\sqrt[3]{bc/a^2}$ where a , b , and c , denoted by blue, red, and green vectors, respectively, are the principal axes in descending order by magnitude of an ellipsoid fit of cell positions for a given rosette) (B, iii), and cell packing [neighbor number determined by Voronoi tessellation (78) (B, iv)]. Dashed lines in B, iv indicate nearest neighbors (gray with black outline) of the cell indicated by the dark gray point. (C) Representative rosettes from 4 to 12 cells per rosette are each shown in 3 roughly orthogonal views. The numbers above each image column indicate the number of cells per rosette. (D) Rosettes transition from an early phase of major shape change (gray background; scaling exponent 7.9 with 95% CI [5.0, 9.8]) to a later phase of approximately isotropic growth (scaling exponent 3.0 with 95% CI [2.7, 3.3]), shown by log-log plot of rosette volume (y axis) vs. maximum rosette width (x axis). (E) Rosettes transition from a relatively flat morphology during the 4- to 6-cell stage (gray background; mean flatness $\cong 0.5$ to 0.7 and mean sphericity $\cong 0.4$ to 0.6, with flatness = 1.0 perfectly flat and sphericity = 1.0 perfectly spherical) to a more spheroidal morphology during the 8- to 12-cell stage (mean flatness $\cong 0.2$ to 0.3 and mean sphericity $\cong 0.7$ to 0.8). (F) Packing increases with cell number at a decreasing rate. D–F depict mean values; error bars indicate SEM. Gray background indicates rosettes of 4 to 7 cells. $n = 100$ rosettes, with ≥ 8 rosettes from each cell-number class, pooled from 3 different samples. (Scale bars, 3 μm .)

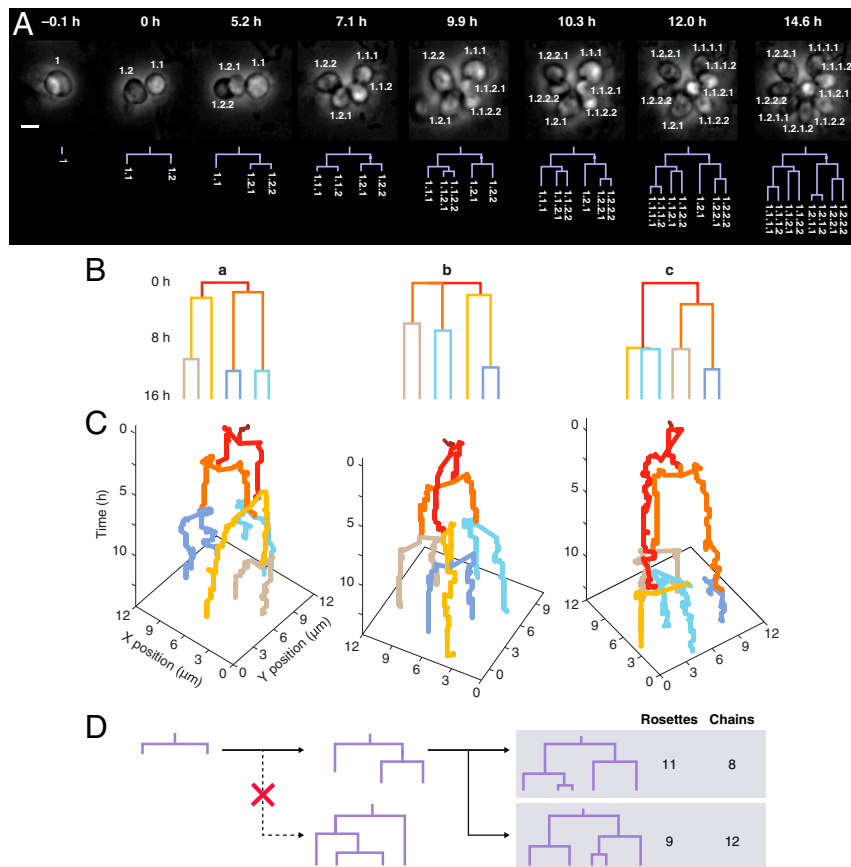


Fig. 3. Variability of developmental dynamics in *S. rosetta*. (A) Lineage analysis for a representative rosette, imaged live by DIC microscopy. Individual daughter cells were marked to record their relationship to their parent lineage (e.g., 1.1 and 1.2 are daughters of cell 1). (Scale bar, 3 μm .) (B) Representative cell lineages illustrating differences in both the order and timing of cell divisions during rosette development. Branch lengths scale with time and are set to zero based on the 1st division. (C) The same lineages displayed as space-time plots to illustrate cell-division variability between rosettes in both space and time. The cells remained in place after divisions, with no large rearrangements, moving apart only slightly as they grew. Colors in B and C indicate the order of cell divisions (red, 1st; orange, 2nd; yellow, 3rd; brown, 4th; light blue, 5th; and darker blue, 6th). (D) Although the order and timing of divisions were variable, cell lineages that formed during rosette and chain development were balanced. In rosettes and chains, imbalanced lineages (i.e., with significantly different numbers of cells) were not observed at any stage (SI Appendix, Fig. S3B). Shown are results for 4- and 5-cell rosettes and chains. "X" indicates a division pattern that was never observed. Data were pooled from 3 independent rosette-induction experiments (for rosettes) and 3 independent experiments with uninduced cells (for chains).

key role in morphogenesis and that the source of the physical constraint in growing rosettes is the ECM, which is known to be required for rosette morphogenesis and connects all cells in a rosette, filling the rosette center (16, 18, 19, 37). Observations of increased cell packing (Fig. 2F) in conjunction with decreasing cellular sphericity (SI Appendix, Fig. S2) were also consistent with the hypothesized increasingly constrained cellular packing as a function of cell number. The phenomenon of physically constrained morphogenesis suggests that the amount of ECM secreted during rosette development is an important factor in sculpting rosette morphogenesis (Fig. 4A and B). We visualized and quantified the volume of the ECM by staining with fluorescein-conjugated Jacalin, a galactose-binding lectin (19, 38). Importantly, Jacalin does not stain chains, so its target is likely specific to rosette ECM (19). We found that the relative amount of space occupied by basal ECM (ECM volume/total cell volume, denoted by ϕ) in developing rosettes was constant and maintained at roughly 6% (Fig. 4C and SI Appendix, Fig. S4). Therefore, we infer that cells in rosettes produce ECM at a constant rate relative to the growth of cells, either through synthesis and secretion alone or through a balance of regulated synthesis, secretion, and degradation.

A key prediction of the ECM constraint hypothesis (Fig. 4A and B) is that compressive stress on cells, balanced by stress in the ECM, should increase with cell number. This predicted increase in residual, compressive stresses on cells in conjunction with increased cell packing could, in part, explain our observations of decreasing cellular sphericity (SI Appendix, Fig. S2). This is reminiscent of an athermal jamming transition in nonliving systems, such as granular materials driven by external stresses that lead to packing (39–41). Biological systems, such as snowflake yeast and microbes proliferating in confined environments (42, 43), also show evidence of jamming, but this time the accumulated stress is due to cellular growth and proliferation, leading to the notion of self-driven jamming (42). Alternatively, cell-cell connections mediated by lateral cell-cell adhesion or cytoplasmic bridges formed during incomplete cytokinesis (Fig. 1B and C and refs. 16 and 37) might be primarily responsible for the structural integrity of rosettes. If cell-cell connections dominate over ECM in holding together rosettes, we would expect cells to be under tension due to stretching of cytoplasmic bridges (37) or due to the forces arising from cell-cell adhesion (44), such that measured stresses would be in the opposite direction to those predicted by the ECM constraint hypothesis (44, 45).

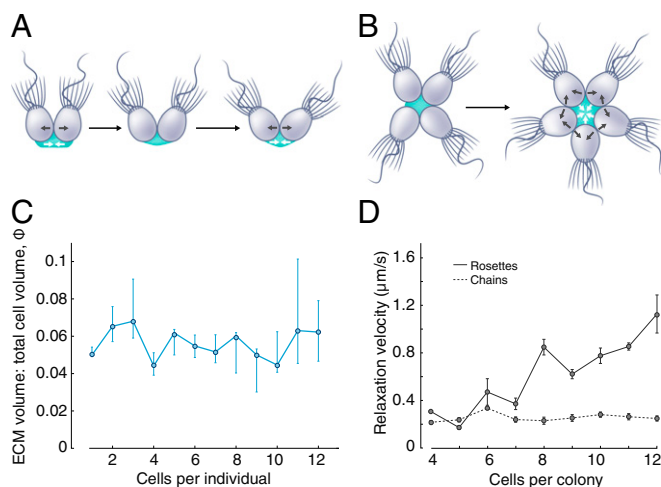


Fig. 4. ECM constrains proliferating cells during rosette morphogenesis. (A and B) Visual summary of the ECM constraint hypothesis. (A) As cells grow, compressive forces exerted on neighboring cells (gray arrows) may be balanced by stress in the basally secreted ECM (cyan), which resists deformation (white arrows). (B) If ECM is limiting, rosettes may undergo a jamming-like transition in which they accumulate residual stress, with cells exerting compressive stresses on one another as they continue to grow and divide, packing into increasingly limited available space. In such a configuration, cells can no longer reorient to adopt a relaxed configuration (as in A). (C) The ratio of total ECM volume to total cell volume as a function of cells per individual (defined as in Fig. 2) is maintained at a constant level throughout rosette development. ECM volume was measured by imaging of rosettes stained with the lectin Jacalin (*SI Appendix, Fig. S4*). Points represent mean values; error bars are bootstrap 95% CIs. $n = 93$ rosettes, pooled from 2 experiments, with ≥ 5 rosettes from each size class. (D) Laser ablation revealed increasing stress as a function of cells per rosette. Single cells in rosettes were ablated, and relaxation velocities were measured by 2D PIV of a single confocal plane through the center of the rosette, giving a lower bound on the maximum relaxation velocity (*SI Appendix, Fig. S5*). Following ablation of a single cell in a rosette, the remaining cells relaxed toward the site of ablation, consistent with the ECM constraint hypothesis. Relaxation velocities increased with increasing cells per rosette (solid line), indicating increasing residual stress as a function of cells per rosette (7, 45, 49), while chains showed no observable relaxation at all cell numbers (dashed line). These ablation results were inconsistent with cytoplasmic bridges or cell-cell adhesion as the dominant factors stabilizing rosette structure, both of which predict relaxation away from the site of ablation in rosettes. Points indicate mean values; error bars indicate SEM. $n = 47$ rosettes pooled from 3 different rosette inductions and $n = 53$ chains from 3 different cultures, with ≥ 4 colonies from each size class.

To probe the balance of forces in developing rosettes, we performed laser-ablation experiments, which provided a readout of the relative magnitude and direction of stresses within rosettes (45–48). Upon ablation of a single cell in a rosette, we found that the remaining cells immediately became more rounded and moved closer together, toward the site of ablation, reducing the size of the gap left by the ablated cell (*SI Appendix, Fig. S5*). This result demonstrated that residual elastic stress, as measured by initial relaxation velocity after ablation (45), is maintained in rosettes, with cells under compressive stress balanced by an additional component of residual stress. Ablation experiments were also performed on chains, which lack the basal ECM of rosettes (16, 18). Consistent with the ECM constraint hypothesis, we observed no relaxation, regardless of cell number (Fig. 4D). While relaxation takes place in 3D, the magnitude of the relaxation velocities in conjunction with the size of rosettes ruled out 3D measurements. Therefore, relaxation velocities were measured by 2D particle image velocimetry (PIV) of a single plane through the center of rosettes (*SI Appendix, SI Materials and Methods and Fig. S5*). Although our measurements may fail to account for out-of-plane components of the relaxation, they provide a lower bound on re-

sidual stress, allowing us to compare the relative magnitude and direction of stresses in rosettes of different sizes.

If rosettes were primarily held together by strong cell-cell adhesion or constrained by cytoplasmic bridges (Fig. 1 B and C), the expected relaxation would have been in the opposite direction, away from the site of ablation, causing a larger gap to open in rosettes, due to cells increasing in contact area with remaining neighbors or surface tension (44) in the former case and tensile stress in bridges in the latter (44–46). Moreover, as the number of cells in rosettes increased, the relative residual stress increased (Fig. 4D), consistent with the ECM constraint hypothesis (Fig. 4 A and B). These results ruled out strong cell-cell adhesion or constraint by cytoplasmic bridges as the dominant physical mechanisms underlying rosette integrity and morphogenesis.

Additionally, residual stress [as measured by initial relaxation velocity (7, 45, 49)] displayed a sharp increase, by nearly a factor of 2, at the 8-cell stage (Fig. 4D), coinciding with the 3D growth transition (Fig. 2 C–E). In conjunction with the observed increase in cell packing (Fig. 2F), this result suggested that the packing of cells is mechanically constrained in developing rosettes such that cells are increasingly compressed against one another with increasing cell number. We reasoned that the shared ECM secreted from the basal end of cells, adhesion to which is likely essential for rosette formation (18, 19), might be the source of this constraint. While we have ruled out bridges as a dominant component of the structural integrity of rosettes, they could play a role in stabilizing cell orientation to hinder out-of-plane growth during the 2D phase of rosette morphogenesis.

Material Properties of ECM Affect Morphogenesis. We next sought to test the ECM constraint hypothesis through perturbative experiments. While the hypothesis entails that changing geometrical properties such as cell shape and relative amount of ECM should have a substantial effect on rosette morphogenesis, these properties could not be experimentally tuned. However, we could perturb the mechanical properties of the ECM. To do so, we treated developing rosettes with strontium chloride (SrCl_2). Strontium is a divalent cation that can stiffen hydrogels, including animal ECM, by increasing cross-linking density (50–54). Importantly, we found that SrCl_2 has no detectable effect on cell growth at up to twice the highest concentration used during this set of experiments (*SI Appendix, Fig. S6*). Under our ECM constraint hypothesis, we predicted that increased ECM stiffness would alter morphogenesis by further constraining cell packing, thus holding cells in a more compact arrangement along with a relative increase in residual stress. Consistent with our hypothesis, we found that rosettes became more compact with increasing SrCl_2 concentration (Fig. 5 A and B and *SI Appendix, Fig. S7*), and the 3D transition shifted to lower cell numbers, occurring at the 5-cell stage for the highest SrCl_2 concentration (Fig. 5C). Additionally, the transition to isotropic growth at the 8-cell stage was abolished (Fig. 5A). Together, these analyses revealed that morphogenesis is altered.

Using laser-ablation experiments, we found that relative residual stress, as determined by maximum initial relaxation velocity, was significantly increased for SrCl_2 -treated 4- to 7-cell rosettes relative to untreated rosettes (Fig. 5D). The increase in residual stress in conjunction with the 2D to 3D growth transition at lower cell numbers supported the hypothesis that ECM-constrained proliferation is a key driver of the 3D transition in rosette morphogenesis. Interestingly, for the 8-cell stage and higher, we did not find a significant increase in residual stress in SrCl_2 -treated rosettes compared to untreated rosettes (Fig. 5D). This is consistent with cells exerting maximum growth pressure on their neighbors at the 8-cell stage and above. Additionally, accumulation of residual stress could be limited by the strength of ECM or cell-ECM adhesion, or cells could actively sense and respond to stresses, such that cells are more likely to leave rosettes by fragmentation, extrusion, or fission in the presence of high stresses. Taken together, these results confirm

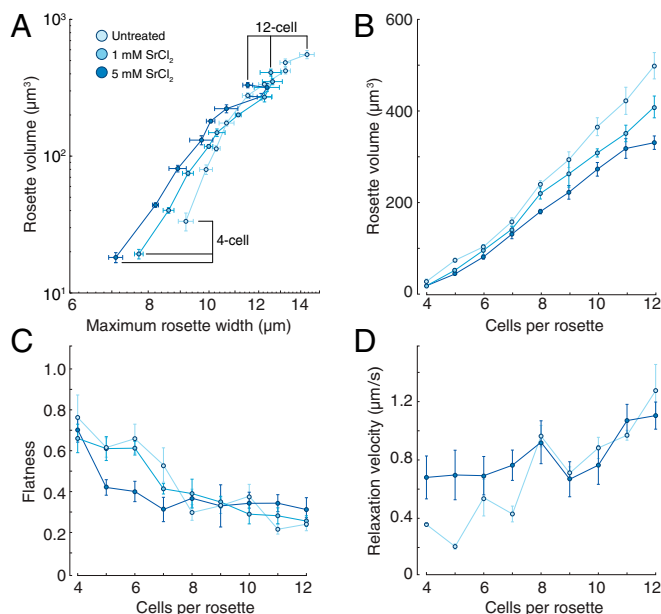


Fig. 5. Material properties of the ECM affect morphogenesis. Treatment of rosettes with SrCl_2 , which stiffens hydrogels by increasing cross-linking density (50–54), alters rosette morphogenesis. (A) Cells were packed more tightly in SrCl_2 -treated rosettes, leading to differences in rosette size and shape (also see *SI Appendix, Fig. S7*). The scaling relationship between maximum rosette width and volume revealed that SrCl_2 treatment abolished the transition to approximately isotropic growth at the 8-cell stage (scaling exponents for ≥ 8 -cell rosettes of 1.1 with 95% CI [0.8, 1.4] and 1.6 with 95% CI [1.2, 2.0] for 1 and 5 mM SrCl_2 treatments, respectively). Log-log plot of rosette volume vs. maximum rosette width represents average values for rosette cell-number classes from 4 to 12 cells per rosette. Error bars are SEM. Rosette volume and maximum width are significantly smaller under SrCl_2 treatment ($P < 0.03$ for either maximum width or volume or both for all rosette cell numbers under both SrCl_2 concentrations with no difference in cell volume; see also B). (B) Rosettes became increasingly compact when treated with increasing concentrations of SrCl_2 , as highlighted by a plot of rosette volume vs. cells per rosette (reanalysis of data from A). While rosette size decreased with increasing SrCl_2 treatment, cell size remained unaffected ($105.9 \pm 8.8 \mu\text{m}^3$, $108.3 \pm 8.0 \mu\text{m}^3$, and $115.3 \pm 5.9 \mu\text{m}^3$ for untreated, 1 mM SrCl_2 , and 5 mM SrCl_2 , respectively, where reported values are mean \pm SEM). Points represent means; error bars are SEM. (C) Quantification of rosette flatness (as in Fig. 1) showed that SrCl_2 shifts the 3D growth transition to lower cell numbers. At the highest SrCl_2 concentration, the transition occurred by the 5-cell stage (compared to untreated rosettes, flatness was found to be significantly lower at the 4-cell stage; $P < 0.03$ by Wilcoxon rank sum tests). For A–C, results were from $n = 100$ rosettes pooled from 3 independent experiments, with ≥ 8 rosettes for each size class for both SrCl_2 concentrations. Data for untreated rosettes were from Fig. 2 D and E. (D) Relative residual stress, as measured by relaxation velocity after laser ablation of single cells (as in Fig. 4D), increased significantly in rosettes of 4 to 7 cells under 5 mM SrCl_2 treatment compared to untreated rosettes ($P < 0.0005$ by Wilcoxon rank sum test). As in the experiments in Fig. 4D, relaxation in SrCl_2 treated cells was always toward the site of ablation, indicating that cells were under compressive stress. These data demonstrate that increased residual stress is correlated with altered rosette morphology. Points represent means; error bars represent SEM from 41 total measurements pooled from 2 experiments, with ≥ 4 rosettes from each size class.

important model predictions by demonstrating that material properties of the ECM can affect morphogenesis, which highlights the central role of the ECM in sculpting rosette morphology.

Amount of ECM, Cell Shape, and ECM Stiffness as Control Parameters for Morphogenesis. To formalize and test our hypothesis of morphogenesis shaped by ECM constraint (Fig. 4 A and B), we next developed a cell-based computational model to simulate rosette development. We used a coarse-grained approximation of the cell

geometry and the main interactions to focus on the primary factors driving colony morphogenesis. In this simplified model of rosette morphogenesis (*SI Appendix, SI Materials and Methods, Simulation Analysis*), there are just 3 dimensionless parameters that control rosette colony shape. These correspond to the geometry of the individual cells, quantified in terms of cell aspect ratio (length along apical/basal axis vs. equatorial diameter), α ; the fraction of the (disordered) ECM relative to total cell volume, ϕ ; and the stiffness of the ECM compared to that of the cells (in terms of the strength of ECM–ECM adhesion bonds relative to the force exerted by growing and dividing cells), σ .

Because development involves few cells (ruling out continuum models) in a low-Reynolds-number environment where inertial forces play a negligible role (55, 56), we developed particle-based simulations akin to Brownian dynamics, but neglected the role of thermal fluctuations, given the large size of the cells and aggregates (51). In the model, the ECM and cells were represented by a system of interacting spherical particles (Fig. 64). This particle representation also allowed us to capture the discrete and variable nature of cell division and the stochastic nature of ECM secretion, as well the polarity of cell division and ECM secretion. Each cell in the model was composed of 3 linked spheres to capture cell shape and for computational tractability, with a small sphere representing the basal pole of the cell, a larger sphere representing the cell body, and the largest representing the collar-exclusion region. Cells interacted sterically with one another. The ECM was modeled as a system of small spheres with attractive interactions in order to capture the complex shapes the ECM can take on (*SI Appendix, Fig. S4*), as well as its deformability. ECM particles similarly shared attractive interactions with the basal poles of cells. Cells in the model were allowed to divide stochastically, with the division plane orientation around the apico-basal axis determined by the previous division (consistent with observations of rosette development from Fig. 3 and ref. 17), and ECM particles were secreted stochastically at a constant rate from the basal pole of nondividing cells (see *SI Appendix, Materials and Methods* for a more detailed description of the model and simulations).

Simulations with parameter values constrained by cell and ECM morphology data collected as part of this study showed that this simple model was sufficient to recapitulate rosette morphogenesis, including the expected 3D transition at the 8-cell stage (*SI Appendix, Fig. S8*). Furthermore, simulations predicted that rosette morphogenesis should be robust to a range of scaled ECM stiffness values (Fig. 6 B–E and *SI Appendix, Fig. S8*) and to the variability of cell divisions (*SI Appendix, Fig. S8*).

Exploration of the effects of different parameter values revealed that the model captures a range of different colonial morphologies (Fig. 6 B and F). This space of forms and associated model parameters constitutes a theoretical morphospace (57) of ECM-based colonial choanoflagellate morphologies. Interestingly, some of the simulated forms resembled colonies, such as tree-like structures [found in *Codosiga cymosa* (58) and an uncharacterized hypothesized *Salpingoeca sp.*; Fig. 6 G, t_2 and t_3] or cups [found in *Codosiga umbellata* (59) and *Salpingoeca monosiera*; Fig. 6 G, c_4 and c_5], that have been reported in other choanoflagellate species (Fig. 6 F and G).

We found that colony morphogenesis was sensitive to all 3 of the dimensionless parameters, changes in each of which can lead to dramatic variations in predicted multicellular forms. For example, holding the other 2 parameters fixed, increase in ϕ alone would be predicted to drive a change from rosettes to disks or cups and from cones to trees (Fig. 6 C and D). This is consistent with our hypothesis that the constraint imposed by relative ECM volume is a key factor in the transition from 2D to 3D morphologies. Colony morphogenesis was also affected by changes in σ ; we found that reduced ECM stiffness is predicted to give rise to disks instead of rosettes (Fig. 6 D and E), which also supports our understanding that the driving factor for rosette formation is the interaction between ECM and cells. Finally, although the effect of changes in α

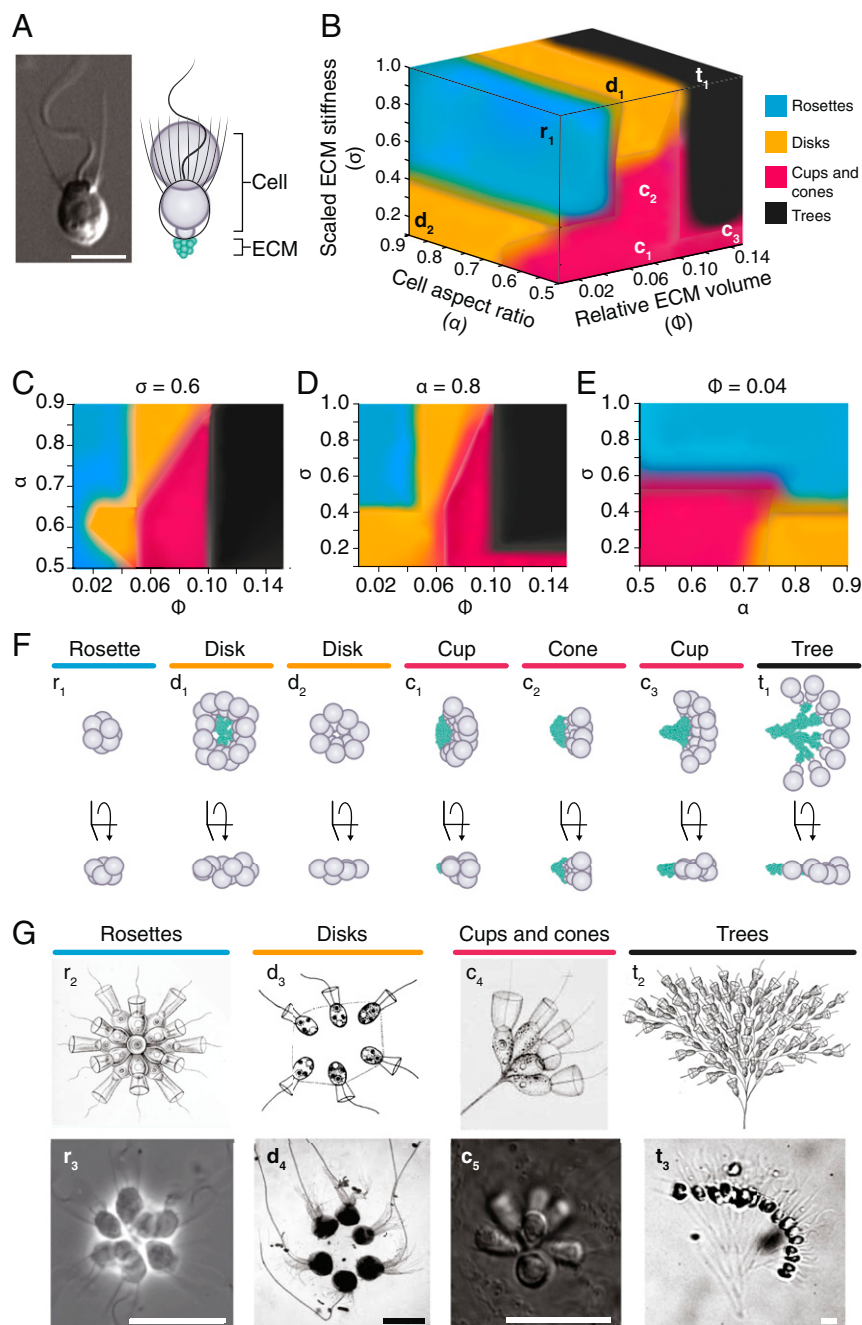


Fig. 6. A simple model shows that amount of ECM, cell aspect ratio, and ECM stiffness tune multicellular morphogenesis. The model incorporates simple cellular and physical interactions, including ECM secretion and cell division, cell–cell steric interactions, and ECM adhesion. Three main parameters describe the system: cell aspect ratio, α ; scaled ECM stiffness, σ ; and relative ECM volume, ϕ . (A) A DIC image of a choanoflagellate (from ref. 16) next to a simulation snapshot to illustrate how cell geometry is modeled by 3 linked spheres (gray), and ECM is modeled by small spheres (green) secreted at the basal pole of cells. In the model, cells interact sterically with one another, and ECM spheres have adhesive interactions with one another and with basal cell particles. (Scale bar, 5 μm .) (B) The morphospace of ECM-based colonial morphologies generated by simulations can be broken into 4 regions: rosettes, disks, cups and cones, and trees. Lowercase letters indicate the region in the morphospace occupied by the corresponding simulated colony in **F**. (C–E) Orthogonal planes through the displayed morphospace, with the parameter of fixed value noted above each plot, illustrate how changing 2 parameters while keeping the 3rd fixed affects morphology. Colors indicate morphological classification as in **B**. (C) Scaled ECM stiffness is constant ($\sigma = 0.6$). (D) Cell aspect ratio is constant ($\alpha = 0.8$). (E) Relative ECM volume is constant ($\phi = 0.04$). (F) Representative simulated colonies for each of the regions are displayed in 2 orthogonal views (r_1 = rosette with $\alpha = 0.7$, $\sigma = 0.8$, and $\phi = 0.04$; d_1 = disk with $\alpha = 0.75$, $\sigma = 0.85$, and $\phi = 0.075$; d_2 = disk with $\alpha = 0.8$, $\sigma = 0.15$, and $\phi = 0.02$; c_1 = cone with $\alpha = 0.55$, $\sigma = 0.5$, and $\phi = 0.08$; c_2 = cup with $\alpha = 0.6$, $\sigma = 0.2$, and $\phi = 0.09$; c_3 = cup with $\alpha = 0.9$, $\sigma = 0.12$, and $\phi = 0.13$; and t_1 = tree with $\alpha = 0.65$, $\sigma = 0.9$, and $\phi = 0.12$). (G) Simulated colonial morphologies are reminiscent of morphologies of colonial choanoflagellates found in nature. r_2 , *Codonosiga botrytis* (79). r_3 , *S. rosetta* (80). d_3 , *Proterospongia haeckelii* (81). d_4 , *Salpingoeca amphoridium* (10). c_4 , *Codosiga umbellata* (59). c_5 , *S. monosiera* (82). t_2 , *Codosiga cymosa* (58). t_3 , Uncharacterized environmental isolate from Curaçao. Reprinted from refs. 58, 59, and 78. Reprinted from ref. 79, which is licensed under CC BY 4.0. Reprinted from ref. 10. Copyright (2008) National Academy of Sciences, U.S.A. Republished from ref. 83 with permission of American Microscopical Society; permission conveyed through Copyright Clearance Center, Inc. (Scale bars, 10 μm .)

was subtler, we saw a clear transition from disks to cups/cones for low values of σ , and for a small range of ϕ , there was also a transition from disks to rosettes, validating our hypothesis that the differences in cell aspect ratio observed across choanoflagellate species can constrain the morphology space accessible to the colony.

Together these results demonstrate that basal secretion of a shared ECM constitutes a robust, yet flexible, mechanism for regulating multicellular morphogenesis. Furthermore, these results made specific predictions about different colony morphologies corresponding to specific cell morphologies and relative ECM volumes and stiffnesses. We did find that simulations failed to recapitulate all aspects of rosette morphogenesis, most saliently, the growth scaling (Fig. 2D) and the absolute magnitudes of flatness and sphericity (Fig. 2E and *SI Appendix*, Fig. S8), likely as our model is a coarse-grained one, although simulations were consistent with SrCl_2 treatment experiments in that increased scaled ECM stiffness was predicted to make rosettes of lower cell number more 3D (*SI Appendix*, Fig. S8). We expect that a more detailed treatment of the mechanics of cells and ECM may capture these aspects of rosette morphogenesis more accurately, but such a detailed model is beyond the scope of the present study.

Discussion

Our quantitative analyses, experimental perturbations, and simulations allowed us to understand the process by which single cells of *S. rosetta* give rise to multicellular rosettes. We found that the earliest stages of rosette morphogenesis proceed through 2D anisotropic growth, which is stereotypically followed by a transition to 3D isotropic growth. In particular, we found that the basal ECM secreted by cells during rosette development physically constrains proliferating cells and thereby drives a stereotyped morphogenetic progression in the absence of strict cell-lineage specification and division timing. Simulations showed that this simple mechanism, the regulated basal secretion of ECM, is sufficient to not only recapitulate rosette morphogenesis, but to yield a morphospace that can not only explain the multicellular morphology of *S. rosetta*, but also that of other species of colonial choanoflagellates. These results emphasize the importance of the choanoflagellate ECM for morphogenesis and should encourage future studies of its composition, physical properties, and regulation.

The importance of the basal ECM revealed in this study may generalize to other choanoflagellate species and colonial morphologies in terms of the 3 dimensionless parameters that characterize the morphospace—the shape of the cells, the amount of the ECM (relative to the cells), and the stiffness of the ECM (relative to that of the cells). Indeed, our simulations predict that differences in ECM levels (resulting from differing rates of biosynthesis, secretion, or degradation), cell shape, and ECM stiffness relative to cells are sufficient to explain the existence of radically different colony morphologies across diverse choanoflagellates. Measurements and comparisons of ECM levels (ϕ), cell shape (α), and ECM stiffness (σ) in diverse colonial choanoflagellates will be crucial to validate the model, and deviations from the predictions of the model could point to additional regulatory mechanisms.

From a broader perspective, rosette morphogenesis shows interesting parallels to mechanisms underlying morphogenesis in diverse other taxa. In terms of physical mechanisms, the constrained proliferation of cells that occurs during rosette development generates crowding stresses like those that regulate morphogenesis by animal epithelia (60, 61), snowflake yeast

(43), and bacterial biofilms (26). In epithelia, compaction of cells due to crowding has been proposed as a general signal for cellular processes underlying tissue homeostasis, such as apoptosis and extrusion (62–65). Further, crowding of proliferating cells can produce a jamming-like behavior, characterized by the accumulation of residual stress (42, 43), that has been proposed as a generic constraint on the development of multicellular systems with fixed cell geometry (43). Due to the generality of physical constraints on cell packing, it is plausible that such phenomena acted both as constraints and regulatory mechanisms in the development and morphogenesis of early animals and their ancestors.

Cellular mechanisms of rosette morphogenesis are also shared with other multicellular systems. Our results demonstrate that the regulation of basal ECM sculpts the multicellular morphology of rosettes. Thus, our biophysical studies have converged on results from genetic screens in *S. rosetta* that implicated animal ECM gene homologs in the regulation of rosette development, including a C-type lectin (18) and predicted glycosyltransferases (19). The basal ECM of rosettes is reminiscent of the basal lamina, a basally secreted layer of ECM that underpins animal epithelia and regulates tissue morphogenesis by constraining cell proliferation (29), including in *Drosophila* wing and egg-chamber development (60, 66, 67), branching growth during lung and salivary-gland development (68, 69), notochord expansion (70), lumen elongation (71), and tumor growth in mammary epithelia (51). The ECM also sculpts morphogenesis in *Volvox*, in which defects in ECM composition disrupt morphogenesis (72, 73), and in bacterial biofilms, in which the ECM can constrain cells and thereby drive 3D morphogenesis (26, 74). Remarkably, some bacteria form multicellular rosettes in a process that is mediated by basal ECM secretion (75, 76).

Altogether, the principles that we can glean from the simplicity of choanoflagellate morphogenesis hold the promise of revealing general principles by which biological and physical mechanisms shape morphogenesis more broadly.

Materials and Methods

See *SI Appendix* for a detailed account of materials and methods. Briefly, *S. rosetta* was grown under standard culture conditions, either as chains or rosettes (18, 23). Rosette development from single cells was induced by the addition of outer membrane vesicles from *A. machipongonensis* (23). Electron microscopy was performed as described (16). The number of cells in rosettes was determined by manual counting. The morphology of rosettes and ECM were quantified from 3D reconstructions of confocal z stacks by using an imaging pipeline developed for this study. Lineage analyses were performed by manually tracking time-lapse phase contrast and differential interference contrast (DIC) images from time-lapse microscopy of developing rosettes and chains. Relaxation velocities were measured by 2D PIV of single confocal planes following laser ablation. Cells and ECM in simulations were modeled as spherical particles with tunable adhesive and repulsive interactions and followed Brownian dynamics (77).

Data Availability. Code for simulations is available at https://github.com/truizherrer/choanoflagellate_colonies. All other data are available upon request.

ACKNOWLEDGMENTS. We thank Kent McDonald and Reena Zalpuri (University of California, Berkeley Electron Microscopy Laboratory) for assistance with transmission electron microscopy sample preparation and imaging; Mary West of the California Institute for Regenerative Medicine/California Institute for Quantitative Biosciences Shared Stem Cell Facility for access to the laser ablation microscope; the late George Oster and Danny Wells for helpful discussions; Debbie Maizels for assistance with the figures; and members of the N.K. laboratory for critical feedback and stimulating discussions.

1. W. Harvey, *Exercitationes de Generatione Animalium: Quibus Accedunt Quaedam de Partu, de Membris ac Humoribus Uteri & de Conceptione* (Typis Du-Gardianis, London, 1651).
2. S. F. Gilbert, *Developmental Biology* (Sinauer Associates, Sunderland, MA, 2000).
3. G. Golling et al., Insertional mutagenesis in zebrafish rapidly identifies genes essential for early vertebrate development. *Nat. Genet.* **31**, 135–140 (2002).
4. Z. Xue et al., Genetic programs in human and mouse early embryos revealed by single-cell RNA sequencing. *Nature* **500**, 593–597 (2013).

5. B.-C. Chen et al., Lattice light-sheet microscopy: Imaging molecules to embryos at high spatiotemporal resolution. *Science* **346**, 1257998 (2014).
6. P. J. Keller, A. D. Schmidt, J. Wittbrodt, E. H. K. Stelzer, Reconstruction of zebrafish early embryonic development by scanned light sheet microscopy. *Science* **322**, 1065–1069 (2008).
7. M. Behrndt et al., Forces driving epithelial spreading in zebrafish gastrulation. *Science* **338**, 257–260 (2012).
8. M. Mayer, M. Depken, J. S. Bois, F. Jülicher, S. W. Grill, Anisotropies in cortical tension reveal the physical basis of polarizing cortical flows. *Nature* **467**, 617–621 (2010).

9. A. Bailles *et al.*, Transcriptional initiation and mechanically driven self-propagation of a tissue contractile wave during axis elongation. *bioRxiv*:430512 (29 September 2018).
10. M. Carr, B. S. C. Leadbeater, R. Hassan, M. Nelson, S. L. Baldauf, Molecular phylogeny of choanoflagellates, the sister group to Metazoa. *Proc. Natl. Acad. Sci. U.S.A.* **105**, 16641–16646 (2008).
11. N. King *et al.*, The genome of the choanoflagellate *Monosiga brevicollis* and the origin of metazoans. *Nature* **451**, 783–788 (2008).
12. I. Ruiz-Trillo, A. J. Roger, G. Burger, M. W. Gray, B. F. Lang, A phylogenomic investigation into the origin of metazoa. *Mol. Biol. Evol.* **25**, 664–672 (2008).
13. B. S. C. Leadbeater, *The Choanoflagellates* (Cambridge University Press, Cambridge, UK, 2015).
14. T. Brunet, N. King, The origin of animal multicellularity and cell differentiation. *Dev. Cell* **43**, 124–140 (2017).
15. B. S. C. Leadbeater, Life-history and ultrastructure of a new marine species of Proterosporgia (Choanoflagellida). *J. Mar. Biol. Assoc. U. K.* **63**, 135 (1983).
16. M. J. Dayel *et al.*, Cell differentiation and morphogenesis in the colony-forming choanoflagellate *Salpingoeca rosetta*. *Dev. Biol.* **357**, 73–82 (2011).
17. S. R. Fairclough, M. J. Dayel, N. King, Multicellular development in a choanoflagellate. *Curr. Biol.* **20**, R875–R876 (2010).
18. T. C. Levin, A. J. Greaney, L. Wetzel, N. King, The Rosetteless gene controls development in the choanoflagellate *S. rosetta*. *eLife* **3**, e04070 (2014).
19. L. A. Wetzel *et al.*, Predicted glycosyltransferases promote development and prevent spurious cell clumping in the choanoflagellate *S. rosetta*. *eLife* **7**, e41482 (2018).
20. J. E. Sulston, E. Schierenberg, J. G. White, J. N. Thomson, The embryonic cell lineage of the nematode *Caenorhabditis elegans*. *Dev. Biol.* **100**, 64–119 (1983).
21. S. P. Leys, A. V. Ereskovsky, Embryogenesis and larval differentiation in sponges. *Can. J. Zool.* **84**, 262–287 (2006).
22. W. H. Lewis, E. S. Wright, *On the Early Development of the Mouse Egg* (Carnegie Institution of Washington, Washington, DC, 1935).
23. R. A. Alegado *et al.*, A bacterial sulfonolipid triggers multicellular development in the closest living relatives of animals. *eLife* **1**, e00013 (2012).
24. A. Woznica *et al.*, Bacterial lipids activate, synergize, and inhibit a developmental switch in choanoflagellates. *Proc. Natl. Acad. Sci. U.S.A.* **113**, 7894–7899 (2016).
25. E. Hannezo, J. Prost, J.-F. Joanny, Theory of epithelial sheet morphology in three dimensions. *Proc. Natl. Acad. Sci. U.S.A.* **111**, 27–32 (2014).
26. J. Yan, A. G. Sharo, H. A. Stone, N. S. Wingreen, B. L. Bassler, *Vibrio cholerae* biofilm growth program and architecture revealed by single-cell live imaging. *Proc. Natl. Acad. Sci. U.S.A.* **113**, E5337–E5343 (2016).
27. T. Savin *et al.*, On the growth and form of the gut. *Nature* **476**, 57–62 (2011).
28. G. Forgács, S. A. Newman, *Biological Physics of the Developing Embryo* (Cambridge University Press, Cambridge, UK, 2005).
29. D. E. Ingber, Mechanical control of tissue morphogenesis during embryological development. *Int. J. Dev. Biol.* **50**, 255–266 (2006).
30. U. Deppe *et al.*, Cell lineages of the embryo of the nematode *Caenorhabditis elegans*. *Proc. Natl. Acad. Sci. U.S.A.* **75**, 376–380 (1978).
31. J. Newport, M. Kirschner, A major developmental transition in early *Xenopus* embryos: I. Characterization and timing of cellular changes at the midblastula stage. *Cell* **30**, 675–686 (1982).
32. D. A. Kane, C. B. Kimmel, The zebrafish midblastula transition. *Development* **119**, 447–456 (1993).
33. B. A. Edgar, P. H. O’Farrell, Genetic control of cell division patterns in the *Drosophila* embryo. *Cell* **57**, 177–187 (1989).
34. K. Bišová, V. Zachleder, Cell-cycle regulation in green algae dividing by multiple fission. *J. Exp. Bot.* **65**, 2585–2602 (2014).
35. J. G. Umen, B. J. S. C. Olson, Genomics of volvocine algae. *Adv. Bot. Res.* **64**, 185–243 (2012).
36. G. Matt, J. Umen, Volvox: A simple algal model for embryogenesis, morphogenesis and cellular differentiation. *Dev. Biol.* **419**, 99–113 (2016).
37. D. Laundon, B. T. Larson, K. McDonald, N. King, P. Burkhardt, The architecture of cell differentiation in choanoflagellates and sponge choanocytes. *PLoS Biol.* **17**, e3000226 (2019).
38. M. C. Roque-Barreira, F. Praz, L. Halbwachs-Mecarelli, L. J. Greene, A. Campos-Neto, IgA-affinity purification and characterization of the lectin jacalin. *Braz. J. Med. Biol. Res.* **19**, 149–157 (1986).
39. C. S. O’Hern, S. A. Langer, A. J. Liu, S. R. Nagel, Random packings of frictionless particles. *Phys. Rev. Lett.* **88**, 075507 (2002).
40. C. S. O’Hern, L. E. Silbert, A. J. Liu, S. R. Nagel, Jamming at zero temperature and zero applied stress: The epitome of disorder. *Phys. Rev. E Stat. Nonlin. Soft Matter Phys.* **68**, 011306 (2003).
41. X. Cheng, Experimental study of the jamming transition at zero temperature. *Phys. Rev. E* **81**, 031301 (2010).
42. M. Delarue *et al.*, Self-driven jamming in growing microbial populations. *Nat. Phys.* **12**, 762–766 (2016).
43. S. Jacobsen *et al.*, Cellular packing, mechanical stress and the evolution of multicellularity. *Nat. Phys.* **14**, 286–290 (2018).
44. M. L. Manning, R. A. Foty, M. S. Steinberg, E.-M. Schoetz, Coaction of intercellular adhesion and cortical tension specifies tissue surface tension. *Proc. Natl. Acad. Sci. U.S.A.* **107**, 12517–12522 (2010).
45. X. Ma, H. E. Lynch, P. C. Scully, M. S. Hutson, Probing embryonic tissue mechanics with laser hole drilling. *Phys. Biol.* **6**, 036004 (2009).
46. M. S. Hutson *et al.*, Combining laser microsurgery and finite element modeling to assess cell-level epithelial mechanics. *Biophys. J.* **97**, 3075–3085 (2009).
47. M. Rauzi, P.-F. Lenne, Cortical forces in cell shape changes and tissue morphogenesis. *Curr. Top. Dev. Biol.* **95**, 93–144 (2011).
48. I. Bonnet *et al.*, Mechanical state, material properties and continuous description of an epithelial tissue. *J. R. Soc. Interface* **9**, 2614–2623 (2012).
49. M. S. Hutson *et al.*, Forces for morphogenesis investigated with laser microsurgery and quantitative modeling. *Science* **300**, 145–149 (2003).
50. C. K. Kuo, P. X. Ma, Ionically crosslinked alginate hydrogels as scaffolds for tissue engineering: Part 1. Structure, gelation rate and mechanical properties. *Biomaterials* **22**, 511–521 (2001).
51. O. Chaudhuri *et al.*, Extracellular matrix stiffness and composition jointly regulate the induction of malignant phenotypes in mammary epithelium. *Nat. Mater.* **13**, 970–978 (2014).
52. E. A. Ryan, L. F. Mockros, J. W. Weisel, L. Lorand, Structural origins of fibrin clot rheology. *Biophys. J.* **77**, 2813–2826 (1999).
53. I. C. Wilkie *et al.*, Mechanical adaptability of a sponge extracellular matrix: Evidence for cellular control of mesohyl stiffness in *Chondrosia reniformis* Nardo. *J. Exp. Biol.* **209**, 4436–4443 (2006).
54. J. Mo *et al.*, Interfibrillar stiffening of echinoderm mutable collagenous tissue demonstrated at the nanoscale. *Proc. Natl. Acad. Sci. U.S.A.* **113**, E6362–E6371 (2016).
55. E. M. Purcell, Life at low Reynolds number. *Am. J. Phys.* **45**, 3–11 (1977).
56. J. L. L. Higdon, The generation of feeding currents by flagellar motions. *J. Fluid Mech.* **94**, 305 (1979).
57. D. M. Raup, Geometric analysis of shell coiling: Coiling in ammonoids. *J. Paleol.* **41**, 43–65 (1967).
58. G. N. Calkins, *Biology* (Henry Holt and Company, New York, 1914).
59. W. Saville-Kent, *A Manual of the Infusoria: Including a Description of All Known Flagellate, Ciliate, and Tentaculiferous Protozoa, British and Foreign, and an Account of the Organization and the Affinities of the Sponges* (David Bogue, London, 1881).
60. L. Hufnagel, A. A. Teleman, H. Rouault, S. M. Cohen, B. I. Shraiman, On the mechanism of wing size determination in fly development. *Proc. Natl. Acad. Sci. U.S.A.* **104**, 3835–3840 (2007).
61. A. E. Shyer *et al.*, Villification: How the gut gets its villi. *Science* **342**, 212–218 (2013).
62. N. I. Petridou, Z. Spiró, C.-P. Heisenberg, Multiscale force sensing in development. *Nat. Cell Biol.* **19**, 581–588 (2017).
63. B. I. Shraiman, Mechanical feedback as a possible regulator of tissue growth. *Proc. Natl. Acad. Sci. U.S.A.* **102**, 3318–3323 (2005).
64. C. Guillot, T. Lecuit, Mechanics of epithelial tissue homeostasis and morphogenesis. *Science* **340**, 1185–1189 (2013).
65. E. Moreno, L. Valon, F. Levillayer, R. Levayer, Competition for space induces cell elimination through compaction-driven ERK downregulation. *Curr. Biol.* **29**, 23–34.e8 (2019).
66. J. C. Pastor-Pareja, T. Xu, Shaping cells and organs in *Drosophila* by opposing roles of fat body-secreted collagen IV and perlecan. *Dev. Cell* **21**, 245–256 (2011).
67. J. Crest, A. Diz-Muñoz, D.-Y. Chen, D. A. Fletcher, D. Bilder, Organ sculpting by patterned extracellular matrix stiffness. *eLife* **6**, e24958 (2017).
68. K. A. Moore *et al.*, Control of basement membrane remodeling and epithelial branching morphogenesis in embryonic lung by Rho and cytoskeletal tension. *Dev. Dyn.* **232**, 268–281 (2005).
69. J. S. Harunaga, A. D. Doyle, K. M. Yamada, Local and global dynamics of the basement membrane during branching morphogenesis require protease activity and actomyosin contractility. *Dev. Biol.* **394**, 197–205 (2014).
70. D. S. Adams, R. Keller, M. A. Koehl, The mechanics of notochord elongation, straightening and stiffening in the embryo of *Xenopus laevis*. *Development* **110**, 115–130 (1990).
71. Q. Li *et al.*, Extracellular matrix scaffolding guides lumen elongation by inducing anisotropic intercellular mechanical tension. *Nat. Cell Biol.* **18**, 311–318 (2016).
72. A. Hallmann, D. L. Kirk, The developmentally regulated ECM glycoprotein ISG plays an essential role in organizing the ECM and orienting the cells of Volvox. *J. Cell Sci.* **113**, 4605–4617 (2000).
73. N. Ueki, I. Nishii, Controlled enlargement of the glycoprotein vesicle surrounding a volvox embryo requires the InvB nucleotide-sugar transporter and is required for normal morphogenesis. *Plant Cell* **21**, 1166–1181 (2009).
74. K. Drescher *et al.*, Architectural transitions in *Vibrio cholerae* biofilms at single-cell resolution. *Proc. Natl. Acad. Sci. U.S.A.* **113**, E2066–E2072 (2016).
75. R. L. Moore, K. C. Marshall, Attachment and rosette formation by hyphomicrobia. *Appl. Environ. Microbiol.* **42**, 751–757 (1981).
76. O. Frank *et al.*, Plasmid curing and the loss of grip—the 65-kb replicon of *Phaebacter inhibens* DSM 17395 is required for biofilm formation, motility and the colonization of marine algae. *Syst. Appl. Microbiol.* **38**, 120–127 (2015).
77. T. Ruiz-Herrero, choanoflagellate_colonies. GitHub. https://github.com/truizherrero/choanoflagellate_colonies. Deposited 3 June 2019.
78. G. Voronoi, Nouvelles applications des paramètres continus à la théorie des formes quadratiques. Premier mémoire. Sur quelques propriétés des formes quadratiques positives parfaites. *J. Reine Angew. Math.* **133**, 97–178 (1908).
79. E. Haeckel, *Kunstformen der Natur* (Verlag des Bibliographischen Instituts, Leipzig, Germany, 1904).
80. D. J. Richter, P. Fozouni, M. B. Eisen, N. King, Gene family innovation, conservation and loss on the animal stem lineage. *eLife* **7**, e34226 (2018).
81. M. Ertl, Zur taxonomie der Gattung Proterosporgia Kent. *Arch. Protistenkd.* **124**, 259–266 (1981).
82. K. H. Hake, “The microbiome of a colonial choanoflagellate from Mono Lake, CA” PhD dissertation, University of California, Berkeley (2019).
83. J. B. Lackey, Morphology and biology of a species of Proterosporgia. *Trans. Am. Microsc. Soc.* **78**, 202–206 (1959).